

# Road anomaly estimation: Model based pothole detection

Zhaojian Li, Ilya Kolmanovsky, Ella Atkins, Jianbo Lu, Dimitar Filev

**Abstract**—This paper describes a model-based pothole detection algorithm that exploits a multi-phase dynamic model. The responses of hitting potholes are empirically broken down into three phases governed by three simpler dynamic system sub-models. Each sub-model is based on a rigid-ring tire and quarter-car suspension model. The model is validated by comparing simulation results over various scenarios with FTire, a commercial simulation software for tire-road interaction. Based on the developed model, a pothole detection algorithm with Unscented Kalman Filter (UKF) and Bayesian estimation is developed and demonstrated.

## I. INTRODUCTION

Potholes are annoying road hazards that can lead to passenger discomfort due to sudden acceleration changes as well as vehicle damages such as tire puncture, suspension damage, steering misalignment, etc. Pothole location information, if available, can be exploited to warn the drivers and plan repairs by the road agencies. The focus of this paper is to develop an onboard pothole detector that is able to detect potholes with commonly available onboard sensors such as speedometers and accelerometers. With a robust detector, pothole locations (e.g., GPS coordinates) can then be automatically sent, processed and shared through the envisioned Vehicle-to-Cloud-to-Vehicle (V2C2V) architecture [1], [2].

Recent studies have focused on pothole detection with mobile agents. Artis *et al* [3] developed a mobile pothole detection algorithm with Android smartphones with accelerometers. Four detection algorithms were proposed which exploit signal processing techniques and have an average true positive rate of around 80 percent. Jakob [4] etc. developed a pothole detector with 3 external accelerometers and machine learning techniques on manually collected data. The detector is implemented in 7 taxis in metropolitan Boston and 39 out of 48 detected potholes were true potholes.

In this paper, we develop a dynamic model to better characterize the responses when hitting a pothole. Unlike previous approaches based on Finite Element Analysis (FEA) [5] which is computationally complex to be used for onboard pothole detection, in this paper, a novel multi-phase dynamic model is built as a multi-mode switching system in which the responses are empirically broken down into phases and each phase is represented by a simpler dynamic model. A pothole

detection algorithm is proposed based on the developed model which exploits Bayesian estimation and the Unscented Kalman Filter.

This paper is organised as follows. The pothole characterization and a multi-phase dynamic model are discussed in Section II. Section III presents the model validation with FTire. A model-based pothole detection algorithm is developed and simulation results are reported in Section IV and Section V concludes the paper.

## II. POTHOLE ANALYSIS AND MULTI-PHASE DYNAMIC MODEL

In the literature on vehicle control with road disturbances, road inputs are often modeled as either deterministic (e.g., given by sinusoids) or stochastic (e.g., given by white noise) without an explicit representation for hitting a pothole [6], [7], [8]. In this paper, we exploit a multi-phase dynamic model for modeling the responses of hitting a pothole.

### A. Pothole characterization

Before we develop our dynamic model, we first analyze pothole geometries on which the dynamic model is based. In this paper, potholes are characterized as *small* or *large* based on whether the tire touches the bottom of the pothole when the vehicle is running over it. For small potholes the tire

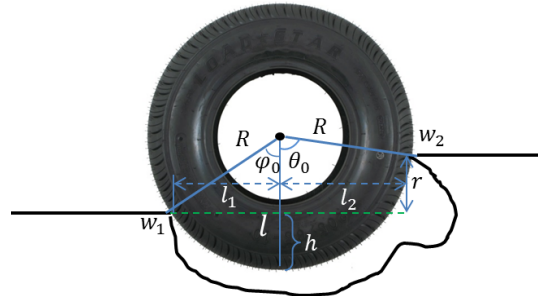


Fig. 1: Small pothole geometry.

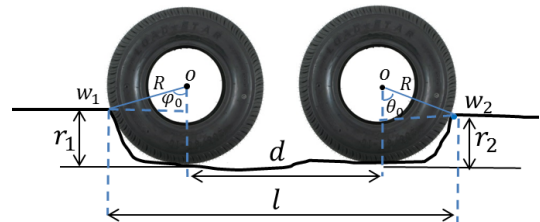


Fig. 2: Large pothole geometry.

will not touch the bottom of the pothole. The geometry of interaction between a wheel and a small pothole at the instant

This work was supported by Ford Motor Company-The University of Michigan Alliance.

Zhaojian Li, Ilya Kolmanovsky and Ella Atkins are with the Department of Aerospace Engineering, The University of Michigan, Ann Arbor, MI 48105, USA {zhaojli, ilya, ematkins}@umich.edu

Jianbo Lu and Dimitar Filev are with Research & Advanced Engineering, Ford Motor Company, Dearborn, MI 48121, USA {jlu10, dfilev}@ford.com

of hitting the rear edge is illustrated in Fig. 1. According to the direction of motion (left to right),  $w_1$  and  $w_2$  are defined as the front and rear edge, respectively. The two main parameters for a small pothole are the diameter of the pothole  $l$  and the vertical difference between the rear and front edges of the pothole  $r$ . Note that in Fig. 1 the height of the rear edge (right) is higher than that of the front edge. Similar analysis can be performed if the front edge is higher than the rear edge. Given the wheel effective radius  $R$ , the following equations are satisfied,

$$\begin{aligned} l &= l_1 + l_2, \\ r &= \sqrt{R^2 - l_1^2} - \sqrt{R^2 - l_2^2}. \end{aligned} \quad (1)$$

From (1),  $l_1, l_2$  can be determined if  $l, r$  and  $R$  are known. Then the angle  $\varphi_0$  in Fig. 1 is

$$\varphi_0 = \sin^{-1} \frac{l_1}{R}. \quad (2)$$

The angle  $\theta_0$  in Fig. 1 can be represented as

$$\theta_0 = \sin^{-1} \frac{l_2}{R}. \quad (3)$$

Note that if the vertical difference between the front and rear edges  $r$  is 0, then

$$l_1 = l_2 = \frac{l}{2}.$$

By large potholes we refer to those with a large diameter such that the wheel will hit the bottom of the pothole when running over it. As illustrated in Fig. 2, the pothole is wide enough that the wheel will touch the bottom of the pothole. In Fig. 2,  $w_1, w_2, l, \theta_0$  and  $\varphi_0$  are defined the same as for the small pothole;  $r_1$  and  $r_2$  are the heights relative to the bottom of the front and rear edge, respectively;  $d$  is the distance of the wheel travelling on the bottom of the pothole. These variables are related as follows,

$$\varphi_0 = \cos^{-1} \frac{R - r_1}{R}, \quad (4a)$$

$$\theta_0 = \cos^{-1} \frac{R - r_2}{R}, \quad (4b)$$

$$d = l - \sin \varphi_0 \cdot R - \sin \theta_0 \cdot R. \quad (4c)$$

With the above variable description, we next develop a dynamic model of a quarter car running over a pothole.

### B. Multi-phase dynamic model

In this paper, the overall response is empirically decomposed into phases and each phase is modeled as a simple dynamic system. The phases are as follows:

- 1) *Rolling on flat ground*: Before hitting the pothole, the vehicle is rolling on flat ground.
- 2) *Rolling about front edge  $w_1$* : The wheel starts to hit the pothole by rolling about the front edge  $w_1$  as in Fig. 1. The wheel drops and  $w_1$  is the only contact point in this phase. During this phase, the angle between  $Ow_1$  and vertical line changes from 0 to  $\varphi_0$ , which is represented in (2).

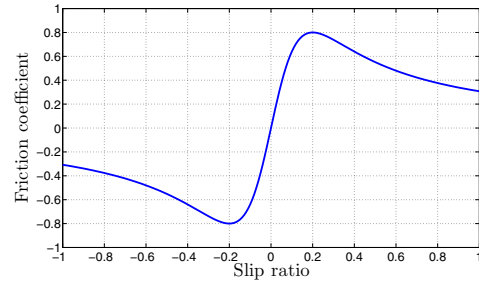


Fig. 3: A typical relation between slip ratio and friction coefficient.

- 3) *Rolling about the rear edge  $w_2$* : The second phase ends when the wheel hits the rear edge of the pothole  $w_2$ .  $w_2$  becomes the only contact point and the wheel is rolling about it. During this phase, the angle between  $Ow_2$  and vertical line changes from  $\theta_0$  to 0.
- 4) *Rolling on flat ground*: After phase 3, the wheel gets out of the pothole and is rolling on flat ground.

The responses of hitting a large pothole are the same as hitting a small one except that the wheel will hit and rolls on the bottom after rolling about  $w_1$  and before hitting  $w_2$ . The responses are also composed of the above basic phases. Since phase 1 and 4 are the same, there are 3 modes (*rolling on flat ground, rolling about front edge and hitting and rolling about rear edge*) corresponding to the distinct phases. The dynamic system models are illustrated in Fig. 4-6.

Since most pothole hitting involves only one wheel at a time, a quarter car model is used. The body of a quarter car is modeled as a rigid body with mass  $m_s$ . Suspension system is modeled as a spring and damper system with constant spring stiffness  $k_1$  and damping coefficient  $c_1$ . The point  $O$  (see Fig. 4-6) is the center of the rim (wheel carrier) and we assume there is no horizontal displacement between rim and the quarter car body. A simplified rigid ring tire model is used where the tire interacts with the rim through a vertical spring and damper system with stiffness  $k_2$  and damping coefficient  $c_2$ , and a horizontal spring and damper system with stiffness  $k_3$  and damping coefficient  $c_3$ . The interaction between the tire and road surface is modeled as a rotating spring and damper through the contact point and the center of wheel rim  $O$  with stiffness  $k_4$  and damping coefficient  $c_4$ . Note that  $w_1$  and  $w_2$  are the only contact points in phase 2 and phase 3, respectively. And  $\theta$  is the angle between the vertical line and the line connecting center of rim  $O$  and the contact point during phase 2 and 3 as in Fig. 5 and Fig. 6.

The  $x_1, x_2, x_3, a$  are the displacements of spring  $k_1, k_2, k_3$  and  $k_4$ , respectively, and these displacements are defined to be positive when the corresponding spring is extended. The  $x_4$  and  $x_5$  are the horizontal and vertical displacements relative to an inertial point;  $\tau$  is the driving torque;  $b$  represents tire-road slip displacement and  $\dot{b}$  is the slip velocity. A commonly used slip-friction relation is illustrated in Fig. 3, which is described by the following expression,

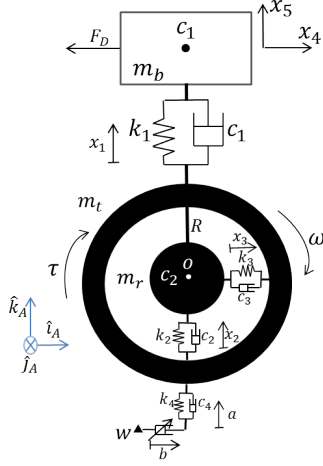


Fig. 4: Dynamic model of running on flat ground.

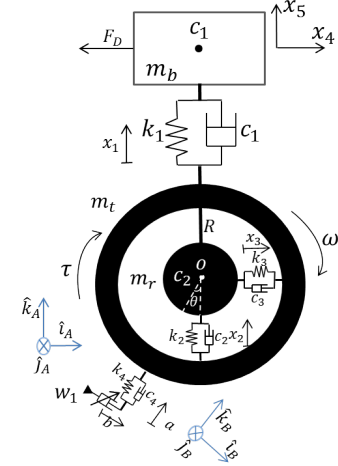


Fig. 5: Dynamic model of running about front edge.

$$\mu(\kappa) = \frac{2\mu_p\kappa_p}{\kappa_p^2 + \kappa^2}\kappa, \quad (5)$$

where  $\kappa$  is the slip ratio and defined as  $\kappa = \frac{v_{sp}}{\max(v_t, \omega R)}$ ,  $v_{sp}$  is the slip velocity and ( $v_{sp} = \dot{b}$  in our case) and  $v_t$  is the wheel tangential velocity. Since we are considering the driving wheel,  $\omega R$  is normally greater than  $v_t$ . As a result, in our formulation we have

$$\kappa = \frac{\dot{b}}{\omega R}. \quad (6)$$

In (5),  $\mu_p$  is the peak friction coefficient which depends on the road material and condition while  $\kappa_p$  is the slip ratio at which the maximum friction coefficient is obtained. In Fig. 3,  $\mu_p = 0.8$  and  $\kappa_p = 0.2$ .  $F_D$  is the longitudinal drag force acting on the quarter car and is modeled as a combination of aerodynamic drag, which is proportional to the square of the speed, and a force due to the rear half car body, which we assume is proportional to the speed, as follows:

$$F_D = \frac{1}{2}C_{ad}v^2 + C_dv, \quad (7)$$

where  $C_{ad}$  is the aerodynamic drag coefficient (incorporating air density);  $C_d$  is a constant capturing the drag force due to the dragging of rear half car body; and  $v$  is the vehicle longitudinal speed.

In phases 2 and 3, we exploit two frames in the derivation of the equation of motions. The first frame,  $F_A$ , is an inertial frame fixed on the ground and the second frame,  $F_B$ , is attached on the wheel. We have  $F_A \xrightarrow[\hat{j}]{\theta} F_B$ , which means  $F_B$  can be obtained by rotating  $F_A$  around the eigenaxis  $\hat{j}$  for  $\theta$ , during phase 2 as in Fig. 5 and  $F_A \xrightarrow[\hat{j}]{-\theta} F_B$ , which means  $F_B$  can be obtained by rotating  $F_A$  around the eigenaxis  $\hat{j}$  for  $-\theta$ , during phase 3 as in Fig. 6. Then Equations of Motions (EoMs) for each phase are as follows:

1. EoMs of mode 1 (phase 1 and 4):

$$\begin{cases} m_b\ddot{x}_5 = -m_bg - k_1x_1 - c_1\dot{x}_1, \\ (m_b + m_r)\ddot{x}_4 = k_3x_3 + c_3\dot{x}_3 - \frac{1}{2}C_{ad}\dot{x}_4^2 - C_d\dot{x}_4, \\ m_r(\ddot{x}_5 - \ddot{x}_1) = -m_rg + k_1x_1 + c_1\dot{x}_1 - k_2x_2 - c_2\dot{x}_2, \\ m_t(\ddot{x}_5 - \ddot{x}_1 - \ddot{x}_2) = -m_tg + k_2x_2 + c_2\dot{x}_2 - (k_4a + c_4\dot{a}), \\ m_t(\ddot{x}_3 + \ddot{x}_4) = -k_3x_3 - c_3\dot{x}_3 + f_\mu, \\ I\ddot{\theta} = \tau - f_\mu(R + a), \\ \dot{a} = \dot{x}_5 - \dot{x}_1 - \dot{x}_2, \\ \dot{b} = \dot{x}_3 + \dot{x}_4 - \dot{\theta}(R + a). \end{cases} \quad (8)$$

2. EoMs of mode 2 (phase 2):

$$\begin{cases} m_b\ddot{x}_5 = -m_bg - k_1x_1 - c_1\dot{x}_1, \\ (m_b + m_r)\ddot{x}_4 = k_3x_3 + c_3\dot{x}_3 - \frac{1}{2}C_{ad}\dot{x}_4^2 - C_d\dot{x}_4, \\ m_r(\ddot{x}_5 - \ddot{x}_1) = -m_rg + k_1x_1 + c_1\dot{x}_1 - k_2x_2 - c_2\dot{x}_2, \\ m_t(\ddot{x}_5 - \ddot{x}_1 - \ddot{x}_2) = -m_tg + k_2x_2 + c_2\dot{x}_2 \\ \quad - \cos(\theta)(k_4a + c_4\dot{a}) - \sin(\theta)f_\mu, \\ m_t(\ddot{x}_3 + \ddot{x}_4) = -k_3x_3 - c_3\dot{x}_3 - \sin(\theta)(k_4a + c_4\dot{a}) \\ \quad + \cos(\theta)f_\mu, \\ I\ddot{\theta} = \tau - f_\mu(R + a), \\ \begin{bmatrix} \dot{a} \\ \dot{b} \end{bmatrix} = \mathcal{R}_r^{-1}(\theta) \begin{bmatrix} -\dot{x}_1 - \dot{x}_2 + \dot{x}_5 \\ \dot{x}_3 + \dot{x}_4 \end{bmatrix} + \begin{bmatrix} \dot{\theta}b \\ -\dot{\theta}(R + a) \end{bmatrix}, \end{cases}$$

where  $\mathcal{R}_r(\theta) = \begin{bmatrix} \cos(\theta) & \sin(\theta) \\ -\sin(\theta) & \cos(\theta) \end{bmatrix}$  is the planar rotation matrix.

3. EoMs of mode 3 (phase 3):

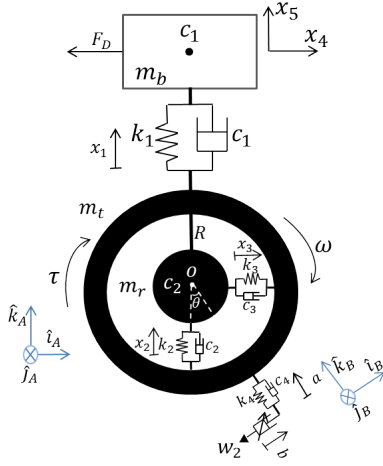


Fig. 6: Dynamic model of hitting and running about rear edge.

$$\begin{cases} m_b \ddot{x}_5 = -m_b g - k_1 x_1 - c_1 \dot{x}_1, \\ (m_b + m_r) \ddot{x}_4 = k_3 x_3 + c_3 \dot{x}_3 - \frac{1}{2} C_{ad} \dot{x}_4^2 - C_d \dot{x}_4, \\ m_r (\ddot{x}_5 - \ddot{x}_1) = -m_r g + k_1 x_1 + c_1 \dot{x}_1 - k_2 x_2 - c_2 \dot{x}_2, \\ m_t (\ddot{x}_5 - \ddot{x}_1 - \ddot{x}_2) = -m_t g + k_2 x_2 + c_2 \dot{x}_2 \\ \quad - \cos(\theta)(k_4 a + c_4 \dot{a}) + \sin(\theta) f_\mu, \\ m_t (\ddot{x}_3 + \ddot{x}_4) = -k_3 x_3 - c_3 \dot{x}_3 \\ \quad + \sin(\theta)(k_4 a + c_4 \dot{a}) + \cos(\theta) f_\mu, \\ I \ddot{\theta} = \tau - f_\mu (R + a), \\ \begin{bmatrix} \dot{a} \\ \dot{b} \end{bmatrix} = \mathcal{R}_r^{-1}(\theta) \begin{bmatrix} -\dot{x}_1 - \dot{x}_2 + \dot{x}_5 \\ \dot{x}_3 + \dot{x}_4 \end{bmatrix} + \begin{bmatrix} -\dot{\theta} b \\ \dot{\theta} (R + a) \end{bmatrix}, \end{cases}$$

where  $\mathcal{R}_r(\theta) = \begin{bmatrix} \cos(\theta) & -\sin(\theta) \\ \sin(\theta) & \cos(\theta) \end{bmatrix}$  is the planar rotation matrix.

The responses of hitting a pothole can then be described by a switching system, for which the switching conditions are determined by the geometries described in (2)-(4). The switching diagram for hitting a small pothole is described in Fig. 7. Before hitting the pothole, the quarter car is rolling on flat ground and the system is in mode 1. When the vehicle starts to contact the pothole, the system switches to mode 2 and the angle described in Fig. 5 changes from 0 to  $\varphi_0$ . The system switches to mode 3 when the wheel hits the rear edge of the pothole and the angle described in Fig. 6 changes from  $\theta_0$  to 0. Then the vehicle rolls on flat ground again and switches back to mode 1.

### III. MODEL VALIDATION WITH FTIRE

The dynamics of hitting a pothole are modeled as a switching system described in Section II. Before we exploit the developed model to implement pothole detection algorithms, we need to tune parameters and validate our model. Towards this end, we use FTire [9], which is a commercial software for tire-road interaction simulation with *Flexible Ring tire model*. It is able to model tire responses to road anomalies such as potholes and speed bumps. We use FTire as the

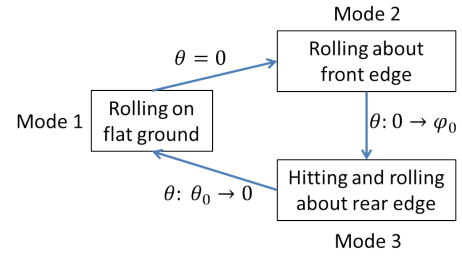


Fig. 7: Switching diagram of hitting a small pothole.

benchmark to validate our model. The FTire simulation setup is illustrated in Fig. 8. Tire type and pothole parameters can be specified in the FTire block set. The inputs of FTire are the three dimensional velocity of the rim center, wheel carrier orientation, driving torque and braking torque. The outputs of the FTire block include three dimensional tire forces, wheel angular velocity, tire deflection, etc. Since our model is two dimensional, to validate our model by comparing the simulation results, we feed longitudinal and vertical tire force components  $F_x$ ,  $F_z$  into a suspension system with same parameters as in the multi-phase model. Then the longitudinal and vertical velocity of the rim center  $v_x$  and  $v_z$  are fed back into FTire to close the loop.

The simulation results of the developed multi-phase model and FTire have been compared for various scenarios, that include varying vehicle speed  $v$ , pothole diameter  $l$  and front/rear edge height difference  $r$ . The simulation results of the two models are similar, see Fig. 9 - Fig. 11. The wheel angular velocity and longitudinal acceleration have more resonance in FTire than our multi-phase model response. The reason is that FTire, unlike our model, uses a Flexible Ring tire model, in which there is a rotational spring and damper between the rim and tire. Fortunately, the detection algorithm we develop next relies more on the trends, which are similar between the two models.

### IV. MODEL-BASED POTHOLE DETECTION

The multi-phase dynamic model developed in Section II and Section III is now exploited to define a pothole detection algorithm.

#### A. Mode confidence

Based on the developed multi-phase model, hitting a pothole is modeled as a switching system with three modes in a certain order. The idea of the detection algorithm is to compare the inferred mode sequence with the expected mode sequence when hitting a pothole. By taking a sequence of measurements  $Y_k = \{y_1, y_2, \dots, y_k\}$  in an interval, the confidence of each mode is computed recursively as follows,

$$\begin{aligned} p(m^j | Y_k) &= \frac{p(y_k | m^j, Y_{k-1}) p(m^j | Y_{k-1}) p(Y_{k-1})}{\sum_i p(y_k | m^i, Y_{k-1}) p(m^i | Y_{k-1}) p(Y_{k-1})} \quad (9) \\ &= \frac{p(y_k | m^j, Y_{k-1}) p(m^j | Y_{k-1})}{\sum_i p(y_k | m^i, Y_{k-1}) p(m^i | Y_{k-1})}, \end{aligned}$$

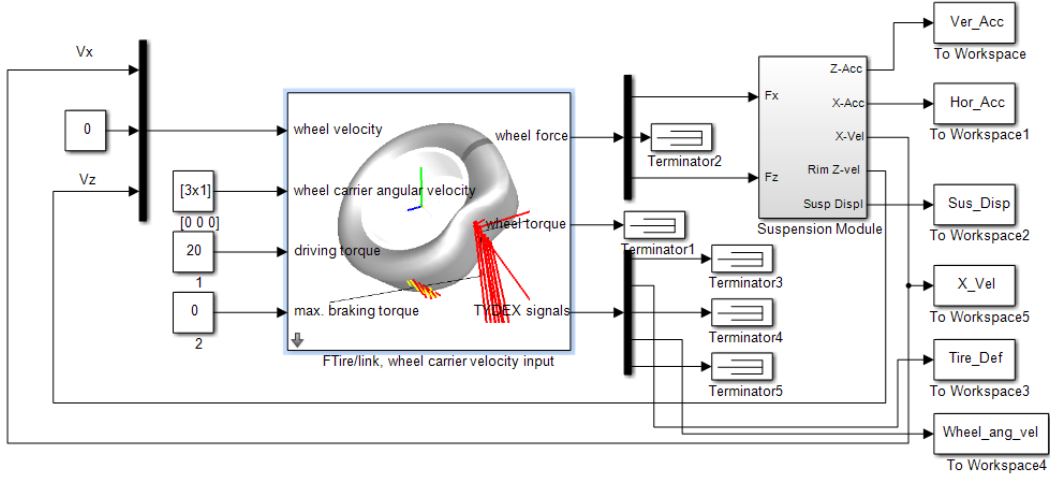


Fig. 8: Simulink setup with FTire.

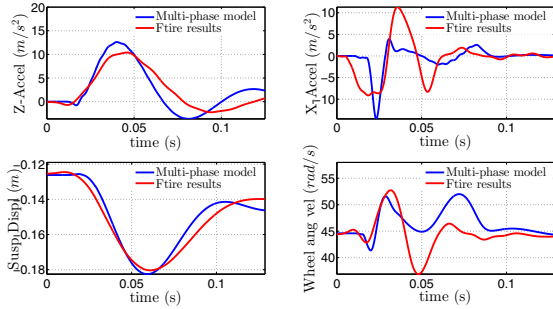


Fig. 9: Responses of multi-phase model vs. FTire:  
 $l = 0.25 \text{ m}$ ,  $r = 0.05 \text{ m}$ ,  $v = 30 \text{ mph}$ .

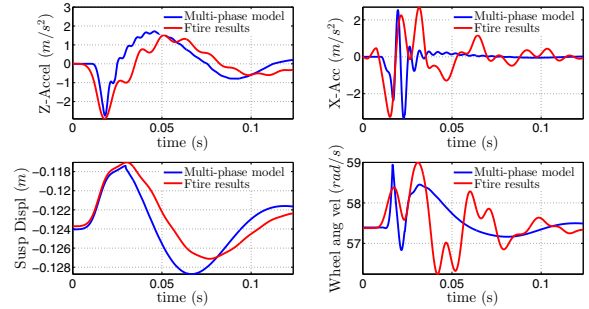


Fig. 11: Responses of multi-phase model vs. FTire:  
 $l = 0.25 \text{ m}$ ,  $r = 0$ ,  $v = 40 \text{ mph}$ .

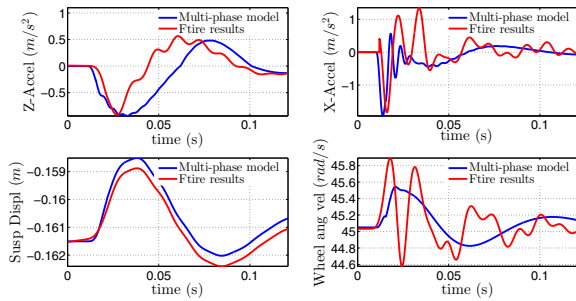


Fig. 10: Responses of multi-phase model vs. FTire:  
 $l = 0.15 \text{ m}$ ,  $r = 0$ ,  $v = 30 \text{ mph}$ .

where  $m^j$  is the  $j$ th mode and  $j = 1, 2, 3$ . The mode with the highest value of the confidence is viewed as the true mode. The difficulty in applying (9) is in computing  $p(y_k|m^j, Y_{k-1})$ , which is the probability of a current measurement  $y_k$  given mode  $m^j$  and the previous observations  $Y_{k-1}$ . In this paper, we exploit Unscented Kalman Filter (UKF) [10] to compute  $p(y_k|m^j, Y_{k-1})$  due to its capacity

for nonlinear estimation and relatively low computation complexity.

#### B. Estimation with UKF

The Unscented Kalman Filter to compute  $p(y_k|m^j, Y_{k-1})$  is based on nonlinear model equations in each mode:

$$\dot{X} = f_i(X, \nu) + \mathbf{w}, \quad (10)$$

$$y = h_i(X, \nu) + \mathbf{v}, \quad (11)$$

where  $X = [x_1, x_2, \dots, a, b, \dot{x}_1, \dot{x}_2, \dot{\theta}]^T$  is the state vector and  $f_i(\cdot)$  is the system equation in mode  $i$  from (8)-(9);  $\nu$  is the vector of the pothole parameters;  $h_i$  is the output function of mode  $i$ ;  $w$  and  $v$  are the process noise and measurement noise, respectively. The UKF (see Fig. 12) uses a deterministic sampling technique referred to as the unscented transform to pick a set of sigmoid points around the mean. These sigma points are then propagated through the system functions and the mean and covariance of the state distribution are estimated from these results. With measurements taken at each step, the UKF recursively



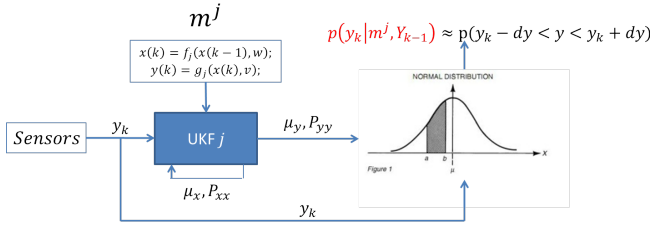


Fig. 12: Estimate  $p(y_k|m^j, Y_{k-1})$  with UKF.

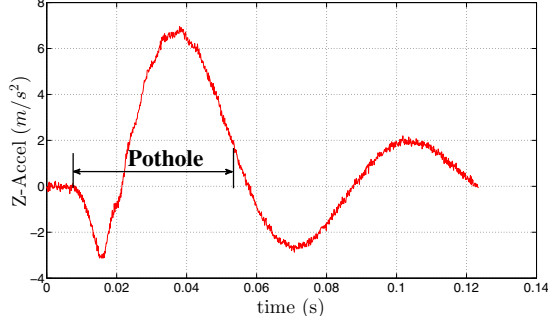


Fig. 13: Fictitious vertical acceleration measurements from FTire.

computes the state mean  $\mu_x$  and covariance  $P_{xx}$ , as well as output mean  $\mu_y$  and covariance  $P_{yy}$ . Assuming that the output is Gaussian, then based on the mean and covariance, the probability density function takes the following form,

$$F_y(y_k) = \frac{1}{\sqrt{(2\pi)^q \det P_{yy}}} \times \exp\left(-\frac{1}{2}(y - \mu_y)^T P_{yy}^{-1}(y - \mu_y)\right), \quad (12)$$

where  $q$  is the dimension of the measurement  $y_k$ . Then by specifying a small  $dy$ ,  $p(y_k|m^j, Y_{k-1})$  can be computed as

$$p(y_k|m^j, Y_{k-1}) \approx p(y_k - dy < y < y_k + dy) \approx 2F_y(y_k)dy. \quad (13)$$

### C. Detection example

In this example, we use horizontal speed  $v_x$ , vertical acceleration  $a_z$  and wheel angular velocity  $\omega$ , which are all commonly accessible measurements in vehicles, for pothole detection. Simulation results from FTire added with Gaussian noise are taken as fictitious measurements. Fig. 13 shows the vertical acceleration simulation results from FTire added with Gaussian noise. The duration of hitting the pothole is illustrated by the double arrow. The mode confidences are computed every 0.01 sec as in (9) and all initialized with 1/3 for the initial probability. The confidence score for every 0.01 s interval is illustrated in Fig. 14. From the results, the second interval is dominated by mode 2 and the following two intervals are dominated by mode 3. Since this sequence matches the formulated switching system in Fig. 7, a pothole is successfully detected.

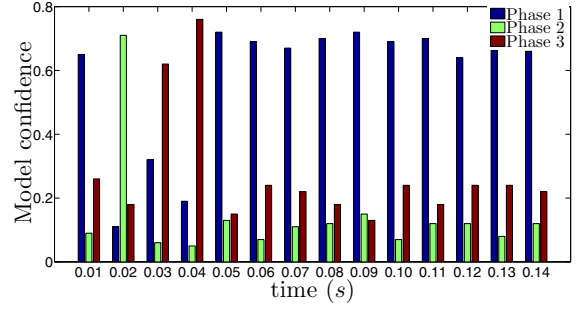


Fig. 14: Mode confidence scores

## V. CONCLUSIONS

In this paper, pothole characteristics were analysed and the dynamics of hitting a pothole by an automotive vehicle were broken down into phases. A multi-phase dynamic model has been built as a switching system with three modes to capture the responses of hitting a pothole. The simulation comparisons between the developed model and FTire were made in various scenarios. The results show that our multi-phase model is able to generate similar simulation results and trends as FTire. A model-based detection algorithm has been proposed by recursively computing the confidence of each mode with Bayesian estimation and the Unscented Kalman Filter.

## REFERENCES

- [1] Z. Li, I. Kolmanovsky, E. Atkins, J. Lu, D. Filev, and J. Michelini, "Cloud aided safety-based route planning," in *2014 IEEE International Conference on Systems, Man, and Cybernetics*, pp. 2525–2530, October 2014.
- [2] Z. Li, I. Kolmanovsky, E. Atkins, J. Lu, D. Filev, and J. Michelini, "Cloud aided semi-active suspension control," in *2014 IEEE Symposium on Computational Intelligence in Vehicles and Transportation Systems*, pp. 76–83, December 2014.
- [3] A. Mednis, G. Strazdins, R. Zviedris, G. Kanonirs, and L. Selavo, "Real time pothole detection using android smartphones with accelerometers," in *Distributed Computing in Sensor Systems and Workshops, 2011 International Conference on*, pp. 1–6, 2011.
- [4] J. Eriksson, L. Girod, B. Hull, R. Newton, S. Madden, and H. Balakrishnan, "The pothole patrol: Using a mobile sensor network for road surface monitoring," in *Proceedings of the 6th International Conference on Mobile Systems, Applications, and Services, MobiSys '08*, (New York, NY, USA), pp. 29–39, ACM, 2008.
- [5] K. Y. Yuan, W. Yuan, J. W. Ju, J. M. Yang, W. Kao, and L. Carlson, "Numerical simulations of mechanical properties of innovative pothole patching materials featuring high toughness, low viscosity nanomolecular resins," *Proc. SPIE*, vol. 8347, pp. 83471B–83471B–7, 2012.
- [6] C. Vassal, S. Savaresi, C. Spelta, O. Senname, and L. Dugard, "A methodology for optimal semi-active suspension systems performance evaluation," in *49th IEEE Conference on Decision and Control*, 2010.
- [7] N. Giorgetti, A. Bemporad, H. Tseng, and D. Hrovat, "Hybrid model predictive control application towards optimal semi-active suspension," in *IEEE ISIE*, 2005.
- [8] R. Miller, "Tuning passive, semi-active and fully active suspension systems," in *Proc. of the 27th Conference on Decision and Control*, 1988.
- [9] Cosin, "Ftire tire software." <http://www.cosin.eu/>, 2014. [Online; accessed 02-Sept-2014].
- [10] S. J. Julier and J. K. Uhlmann, "Unscented filtering and nonlinear estimation," *Proceedings of the IEEE*, vol. 92, pp. 401–422, Mar. 2004.